Hindawi
Advances in Civil Engineering
Volume 2021, Article ID 8863136, 21 pages
https://doi.org/10.1155/2021/8863136

Research Article

Study the Fire Resistance of Desert Sand Concrete (DSC) with Interface Phase through Uniaxial Compression Tests and Analyses

Qian Zhang[1], **Haifeng Liu**[1,2], **Qiang Liu**[1], **Jialing Che**[1], **Weiwu Yang**[1], **Jurong Ma**[2], **Shu Ing Doh**[3], **and Kar Sing Lim**[3]

[1]*College of Civil and Hydraulic Engineering, Ningxia University, Yinchuan 750021, China*
[2]*Xinhuan College, Ningxia University, Yinchuan 750021, China*
[3]*College of Engineering, University Malaysia Pahang, Lebuhraya Tun Razak, Gambang 26300, Kuantan, Pahang, Malaysia*

Correspondence should be addressed to Haifeng Liu; liuhaifeng1557@163.com

Received 20 August 2020; Revised 1 February 2021; Accepted 13 February 2021; Published 25 February 2021

Academic Editor: Andreas Lampropoulos

The shortage of sand resources and high-rise building fires are becoming increasingly prominent. Desert sand (DS) with smaller particles can effectively fill the concrete voids and further improve its working performance; it is used as a fine aggregate to produce concrete. This article studied the performance of desert sand concrete (DSC) against fire resistance by using mathematical modeling for simulation. The stress-strain curves of desert sand mortar (DSM) after elevated temperatures were tested, and the constitutive model was established. By comparing the experiment and simulation results, it was verified that the model is suitable to be adopted in this study. Data from experiment and past literature can serve as parameters for the subsequent simulation. The destruction process of DSC under uniaxial compression after elevated temperature was simulated by using ANSYS. The simulation results indicated that, after elevated temperature, compressive strength reduced with increase of interface thickness. The compressive strength of DSC had a substantially linear increase as the interface compressive strength increased. For two-grade coarse aggregate, the optimum volume content was 45%, and particle size of it showed a significant effect on the compressive strength of DSC. The DSM constitutive model and simulation results can provide a sound theoretical basis and technical support for DSC engineering applications.

1. Introduction

In recent years, the incidence of fires has soared in China. Fire disasters of high-rise buildings were recorded at alarming rates of 2499 cases in 2013 [1] (p. 329), 4989 in 2014 [2] (p. 365), and 5571 in 2015 [3] (p. 303). Compared to 2013, the fire growth rates in 2014 and 2015 were 99.64% and 122.93%, respectively. For high-rise buildings, due to the chimney effect, fire spreads rapidly, which may cause an increase in economic losses and casualties. Therefore, research on the fire resistance of concrete buildings after elevated temperature will help reduce unnecessary damage. Numerous researchers studied concrete after different elevated temperatures [4–7]. Pliya et al. [6] heated the recycled aggregate high-strength concrete to 550–600°C at different heating rates and observed a decline in compressive strength. Qiu [7] used a test to study C70 concrete failure behaviour after heating of 25–800°C. Initial crack toughness and instability toughness both decreased with temperature increase. In this paper, the target temperatures were set at 300°C, 500°C, and 700°C, while the room temperature (20°C) was used as a reference.

Due to rapid development of construction and infrastructure, the shortage of medium sand in construction has become a global problem. Many researchers in China and abroad have started to find alternatives to substitute construction sand [8–10]. To reduce the dependency on nonrenewable sources while curbing environmental pollutions, desert sand was used as a substitute for medium sand. Many researchers are working on DSC [11–13]. The fineness modulus of DS is only 0.292, which is finer than fine sand (0.7–1.5 mm). It is classified as ultrafine sand. Zhang and

Yang [14] used Mu Us DS and Tengger DS to produce DSC and suggested that DS could be used as fine aggregate for concrete production. Wang and Li [15] revealed that high-strength prestressed concrete of C50 [16] could be produced by mixing DS and medium sand. Thus, the use of desert sand can be widely applied for civil engineering near the desert region for better economic and social benefit. Yan et al. [17] applied statistical models to optimize the mix ratio for DSC, which replaced medium sand with a different proportion of DS obtained from Mu Us region.

The macrolevel for concrete is an important aspect of concrete study. Concrete damage usually leads to a loss of concrete capacity. Concrete macroscopic failure is closely linked to nonuniformity of its microstructure. From macroscopic structure perspective, many investigations have been conducted to develop the mechanical models of concrete [18–21]. By modifying Drucker-Prager model, Yu et al. [18] proposed a new coupling function of concrete strength, which included temperature and strain rate in the model. Marsavina et al. [19] used transient finite element analysis to analyse chloride penetration in concrete. Albrifkani and Wang [20] proposed an explicit dynamic finite element simulation method to predict the nonlinear response of axial and rotational constraints of reinforced concrete beams at different temperatures. Morales-Alonso et al. [21] concluded that the high accuracy between experimental and simulated data can be produced using a cohesive crack model to study the fracture behaviour of concrete.

Concrete was a three-phase mixture; as one phase of concrete, ITZ was also called interface phase [22]. Due to the large porosity, low strength, and heterogeneity in interface phase, interface phase became the weakest bond in concrete [23, 24], and the thickness was usually approximately 10–50 μm [25]. Scrivener et al. [26] suggested that the interface phase was a gradual transition region and was highly heterogeneous. Jin et al. [27] highlighted the influence of concrete compressive load based on one-way coupling of heat and force. Through Monte Carlo simulation, the impact of graded aggregate geometric characteristics on interface phase fraction was studied [28]. Thus, a further study of concrete interface phase is necessary.

A lot of researchers have conducted many studies on mechanical properties of concrete. Nonetheless, few studies of DSC with interface phase after elevated temperature have been reported. Many existing models were relatively complicated and not suitable for DSC after elevated temperature. Considering the limitations of experiment, based on a random aggregate model, DSC was divided into coarse aggregate, DSM, and interface. The failure process of DSC under uniaxial compression after elevated temperature was simulated by using ANSYS. The effects of interface phase thickness, interface phase compressive strength, specimen size, coarse aggregate volume content, and particle size on compressive strength of DSC after elevated temperature treatment were analysed. Numerical simulation research can provide a support for DSC fire resistance after elevated temperature.

2. DSM Test

2.1. Materials of DSM Test. To simulate compressive strength of DSC, it is necessary to perform a uniaxial compressive test on DSM for validation purposes. Tables 1–5 show the physical and chemical indexes of materials used in the study.

Figure 1 shows the sieving curves of test materials. It was observed that the passing rate for DS was 100%, while it was only 55% for medium sand. Therefore, the particle size of DS was much smaller than that of medium sand. The *w/c* ratio of 0.45, cement-sand ratio of 0.5, and 0.3% superplasticizer of the cementitious materials were designed. A total of 10% fly ash was used to replace cement, while the medium sand was replaced with desert sand replacement rates (DSR) of 20%, 40%, 60%, 80%, and 100%.

2.2. DSM Test. The production of DSM specimens was carried out by complying with JCJ/T 70-2009 [29]. The test specimen was a prism of $40 \times 40 \times 160$ (mm^3). DSM with different DSR was heated at 300°C, 500°C, and 700°C for 3 hours. After the heating process, the specimens were cooled by natural cooling. From the test, the surface colour of DSM changed from dark grey to light grey with an increase of DSR. Besides that, the colour of specimen changed from red to white, as the temperature increased from 500°C to 700°C. Sun and Liu [30] have conducted an experiment of DSC using the same material. After elevated temperature, compared with the surface colour of test specimen at room temperature, it was found that the surface colour of test specimen at 500°C was pale and yellow, and the surface of test specimen at 700°C was grayish-yellow. The colour change was due to the presence of FeO in desert sand, which was roughly twice of FeO in medium sand. From Table 2, it was observed that FeO content in DS was approximately twice as that in medium sand. The relative amount of DS in DSM changed the specimens colour. Xu et al. [31] found that the colour of recycled mortar after elevated temperature changed from grey to light red and grey. The result was consistent with the findings of this research.

The uniaxial compression test of specimen was performed by using CMT5305. The loading rate was 0.006 mm/s, and it was controlled by displacement. During the test, strain gages were fixed at both horizontal and vertical directions perpendicular to one another at the front and back surface of the specimen. Figure 2 shows the details of the test setup.

Figure 3 shows the specimen failure characteristics of DSM with different DSR. It was observed that when specimen was compressed, part samples cracks started at the specimen edge and were destroyed along the diagonal direction, while the physical observation of the other damaged specimens showed

Table 1: Physical and mechanical indexes of sands.

Material	Fineness modulus (%)	Bulk density ($g{\cdot}cm^{-3}$)	Apparent density ($g{\cdot}cm^{-3}$)	Mud content (%)	Void ratio (%)
National standard (medium sand)	2.3~3.0	≥1350	≥2500	≤1.0	≤47
Medium sand (artificial sand washing)	2.38	1570	2636	0.7	41.9
Desert sand (Mu Us desert sand)	0.29	1400	2624	0.14	40.95

Table 2: Chemical components of sands.

Material	Component (%)							
	Al_2O_3	CaO	FeO	MgO	SiO_2	K_2O	Na_2O	Loss on ignition
Medium sand	9.74	0.96	0.98	1.09	86.55	—	—	—
Desert sand	8.72	2.00	1.85	1.51	82.66	0.12	0.07	2.8

Table 3: Physical indexes of cement.

Cement type	Fineness	Standard consistency water consumption (%)	Stability	Setting time (min)		Compressive strength (MPa)	
P.O 42.5 R	4.7	28	Aptitude	135 (initial)	174 (final)	33.4 (3d)	54.8 (28d)

Table 4: Physical indexes of fly ash.

Level (I)-fly ash	Water content (%)	Fineness (45 μm sieve residue) (%)	Water demand ratio (%)	SO_3 (%)	Loss on ignition (%)
Standard value	≤1	≤12	≤95	≤3	≤5
Measurements	0.2	9.2	94	0.2	2.8

Table 5: Test results of water (tap water) quality.

Test items	Prestressed concrete	RC	Plain concrete	Detection value
pH value	≥5.0	≥4.5	≥4.5	7.70
Insolubles ($mg{\cdot}L^{-1}$)	≤2000	≤2000	≤5000	32.65
Solubles ($mg{\cdot}L^{-1}$)	≤2000	≤5000	≤10000	40.32
Cl– ($mg{\cdot}L^{-1}$)	≤500	≤1000	≤3500	18.92
SO_4^{2-} ($mg{\cdot}L^{-1}$)	≤600	≤2000	≤2700	23.74
Alkali content ($mg{\cdot}L^{-1}$)	≤1500	≤1500	≤1500	10.34

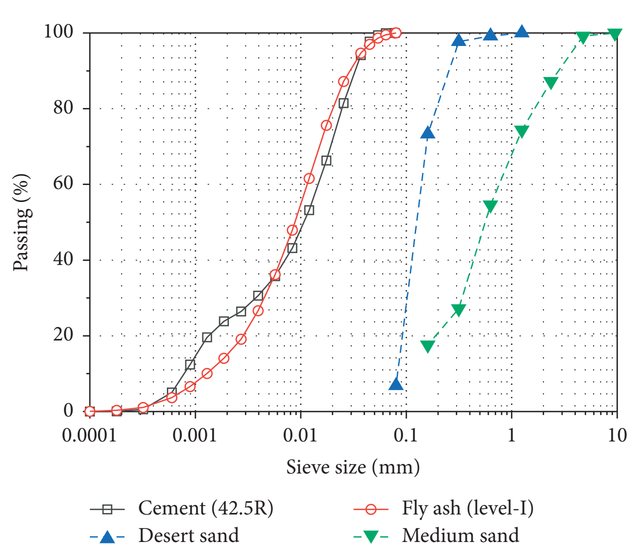

Figure 1: Sieving curve of the test materials.

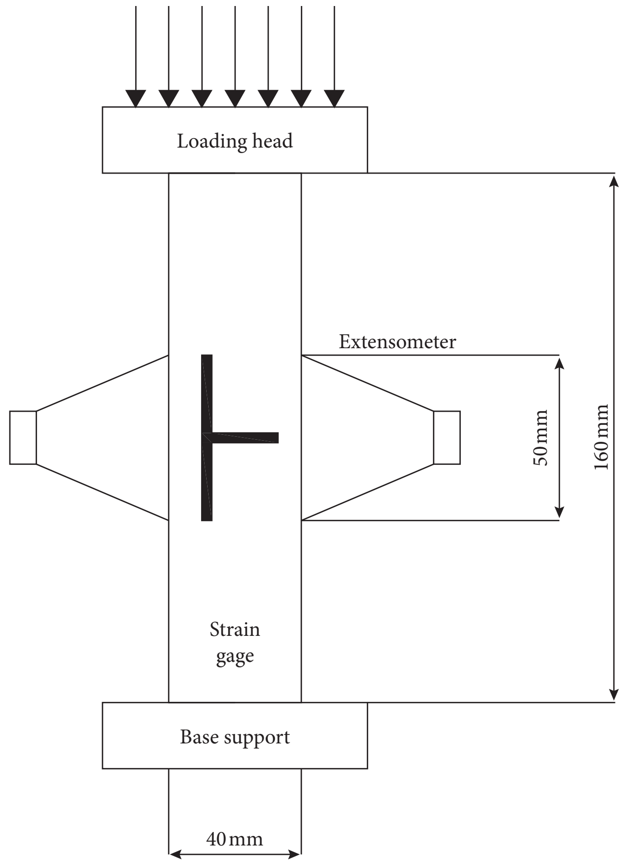

Figure 2: Loading setup.

(a)

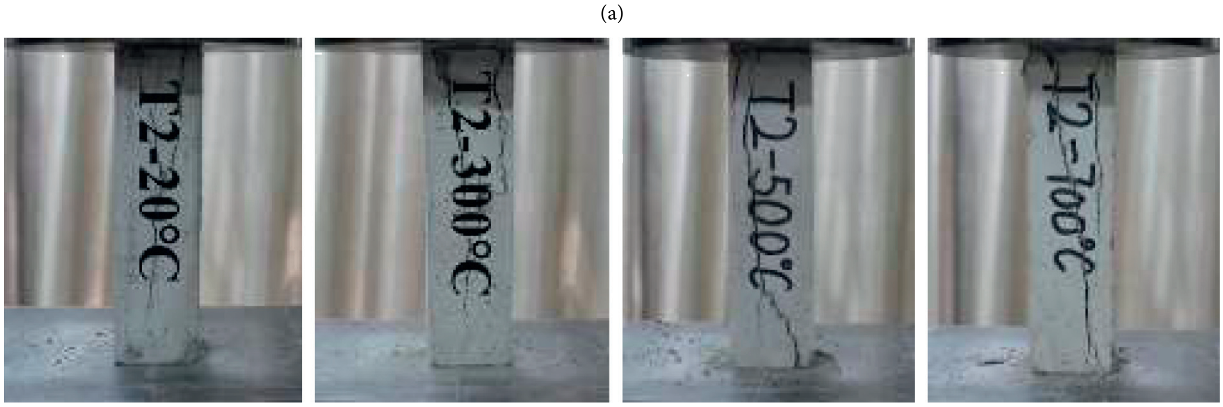

(b)

Figure 3: Continued.

Figure 3: Compression failure of DSM specimens after elevated temperature. (a) DSR-0%; (b) DSR-20%; (c) DSR-40%; (d) DSR-60%; (e) DSR-80%; (f) DSR-100%.

that samples failed obliquely at different angles to the specimens centre and then cracked downward forming a Y-shape.

After elevated temperature, the DSM underwent crushing with different damage degrees. Figure 4 shows the increase of failure angle with increasing temperature. It was found that the cones at 300°C, 500°C, and 700°C were relatively small as compared with the cone at room temperature. As temperature increases, the structure integrity was gradually deteriorated, and the overall structure was relatively loose at 700°C. This phenomenon was mainly caused by the moisture evaporation inside the concrete, C⟶S⟶H gel dehydration and decomposition, and CH chemical decomposition, as temperature rose from room temperature to 700°C [32].

2.3. Test Results of Uniaxial Compression Performance of DSM. The stress-strain curves of DSM with different DSR after elevated temperature were obtained through experimental research. Figure 5 shows the DSM with DSR of 0% (ordinary mortar) and 100% (pure desert sand mortar) after elevated temperature. As shown in Figure 5, the peak stress of pure DSM at 300°C increased by about 5% in comparison with ordinary mortar. Meanwhile, the peak stress of pure DSM at room temperature, 500°C, and 700°C was lower than that of ordinary mortar. The optimal DSR was 40%. The peak stress, peak strain, elastic modulus, and Poisson's ratio of DSM can be obtained from Figure 5. The secant modulus at 40% peak stress was taken as elastic modulus, and ratio of transverse strain to longitudinal strain at elastic stage of stress-strain curve was regarded as Poisson's ratio.

According to the test results, the fitting relationship of DSM after elevated temperature is obtained. The determination coefficients (R^2) of equations (1)–(4) were larger than 0.96. The fitting equations (1)–(4) were as follows:

$$\frac{\sigma_c(S,T)}{\sigma_c} = 0.99 + 0.182\left(\frac{T-20}{700}\right) + 0.33S + 0.018S\left(\frac{T-20}{700}\right) - 0.666\left(\frac{T-20}{700}\right)^2 - 0.394S^2, \quad (1)$$

$$\frac{\varepsilon_c(S,T)}{\varepsilon_c} = 0.997 + 0.51\left(\frac{T-20}{700}\right) - 0.279S - 0.118S\left(\frac{T-20}{700}\right) + 0.685\left(\frac{T-20}{700}\right)^2 + 0.145S^2, \quad (2)$$

$$\frac{E(S,T)}{E} = 1.02 - 1.385\left(\frac{T-20}{700}\right) + 0.167S + 0.036S\left(\frac{T-20}{700}\right) + 0.487\left(\frac{T-20}{700}\right)^2 - 0.185S^2, \quad (3)$$

$$\frac{\nu(S,T)}{\nu} = 0.99 + 0.55\left(\frac{T-20}{700}\right) - 0.13S + 0.06S\left(\frac{T-20}{700}\right) - 4.28\left(\frac{T-20}{700}\right)^2 - 0.02S^2 + 3.61\left(\frac{T-20}{700}\right)^3, \quad (4)$$

where $\sigma_c(S,T)$, $\varepsilon_c(S,T)$, $E(S,T)$, and $\nu(S,T)$ are the peak stress, peak strain, elastic modulus, and Poisson's ratio of DSM after elevated temperature; σ_c, ε_c, E, and ν are the peak stress, peak strain, elastic modulus, and Poisson's ratio of ordinary mortar at room temperature; T is temperature; S is the DSR.

Based on the model [33], which belonged to concrete and mortar in Figure 6, the DSM stress-strain curve after elevated temperature can be obtained by test and was fitted, and the fitting results agree well, as shown in Figure 7.

Therefore, equation (5) was suitable for DSM after elevated temperature in this study.

$$\frac{\sigma}{\sigma_c} = \frac{n\varepsilon}{\varepsilon_c}\left[n - 1 + \left(\frac{\varepsilon}{\varepsilon_c}\right)^{-n}\right]. \quad (5)$$

The parameter n was obtained by fitting, which was the function of DSR, S, and temperature T. The range of T was 20–700°C. The coefficient of determination (R^2) of equation (6) was 0.956, and the fitting was good. The fitting equation was as follows:

$$n = 1.748 + 14.383\left(\frac{T-20}{700}\right) + 1.46S + 3.31S\left(\frac{T-20}{700}\right) - 9.718\left(\frac{T-20}{700}\right)^2. \quad (6)$$

3. Computational Model of DSC

3.1. Material Model and Failure Criteria

3.1.1. Constitutive Model and Parameters of Coarse Aggregate after Elevated Temperatures. The elevated temperature had a little negative effect on coarse aggregates. The coarse aggregate was hardly damaged during loading process. Concrete damage was mainly due to the insufficient bearing capacity of mortar. Thus, the elastoplastic model of coarse aggregate as shown in Table 6 was selected.

3.1.2. Parameters of Interface Phase after Elevated Temperatures. Interface phase was the weakest phase in the overall structure of concrete. It will affect the concrete strength. The corresponding parameters of interface phase were relatively small as compared with mortar strength and elastic modulus. Generally, the elastic modulus of interface phase was within 30–70% of mortar elastic modulus [35, 36]. Based on the mortar mechanical parameters, the strain and Poisson's ratio were kept constant, and the stress and elastic

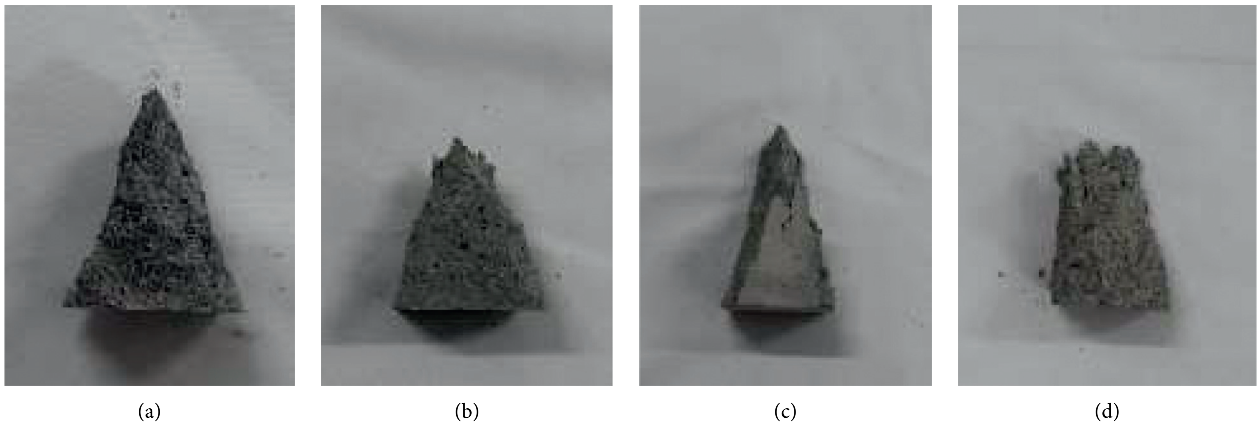

Figure 4: Destruction of DSM after elevated temperature. (a) Room temperature; (b) 300°C; (c) 500°C; (d) 700°C.

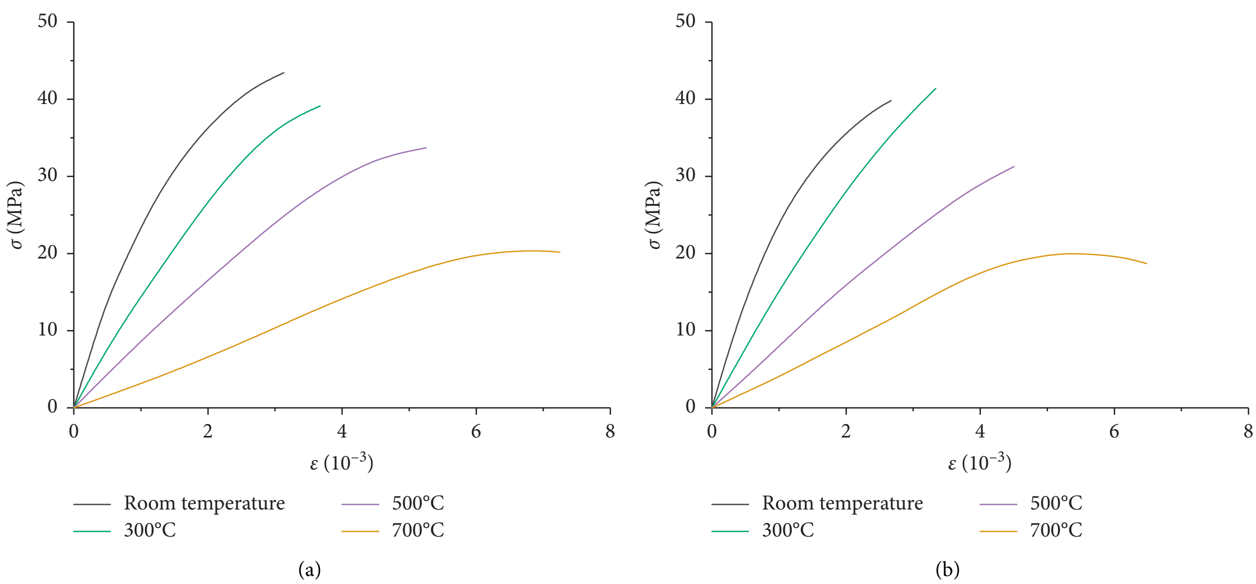

Figure 5: Stress-strain curve of DSM after elevated temperature. (a) DSR-0%; (b) DSR-100%.

modulus were multiplied by a coefficient (<1) as the stress and elastic modulus of interface phase. In this study, the mortar elastic modulus was taken as the interface phase elastic modulus according to an arithmetic sequence of 60%, 70%, 80%, and 90%, respectively.

3.1.3. Failure Criteria. Concrete was generally regarded as a brittle material, and only a small deformation under external force may cause the component to break and fracture. In this study, the maximum principal strain failure criterion was adopted. When the strain value of finite element unit reaches the maximum principal strain value, the unit is regarded as a failure and cannot continue to bear the load.

3.2. Material Model and Failure Criteria

3.2.1. Random Aggregate Model. Fuller and Thompson [37] proposed a maximum compactness rational grading curve to achieve best compactness and strength. The Fuller-grading curve expression was as follows:

$$P = 100\%\left(\frac{D_h}{D_{\mathrm{MAX}}}\right)^{0.5}, \tag{7}$$

where D_h is screen hole diameter; P is percentage of coarse aggregate passing diameter D_h; D_{MAX} is coarse aggregate maximum particle size.

Based on Fuller-grading curve, Walaraven and Reinhardt [38] converted a three-dimensional grading curve into

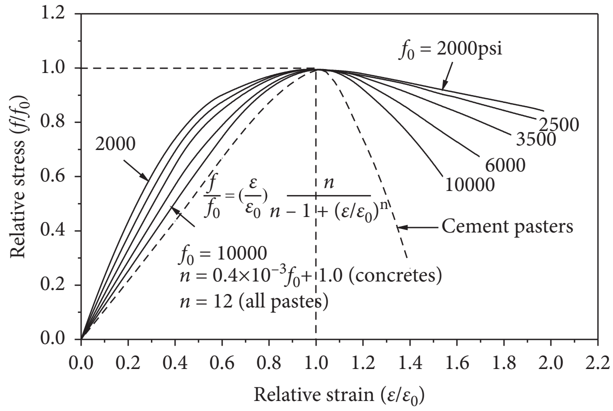

Figure 6: Constitutive model of concrete and mortar [33].

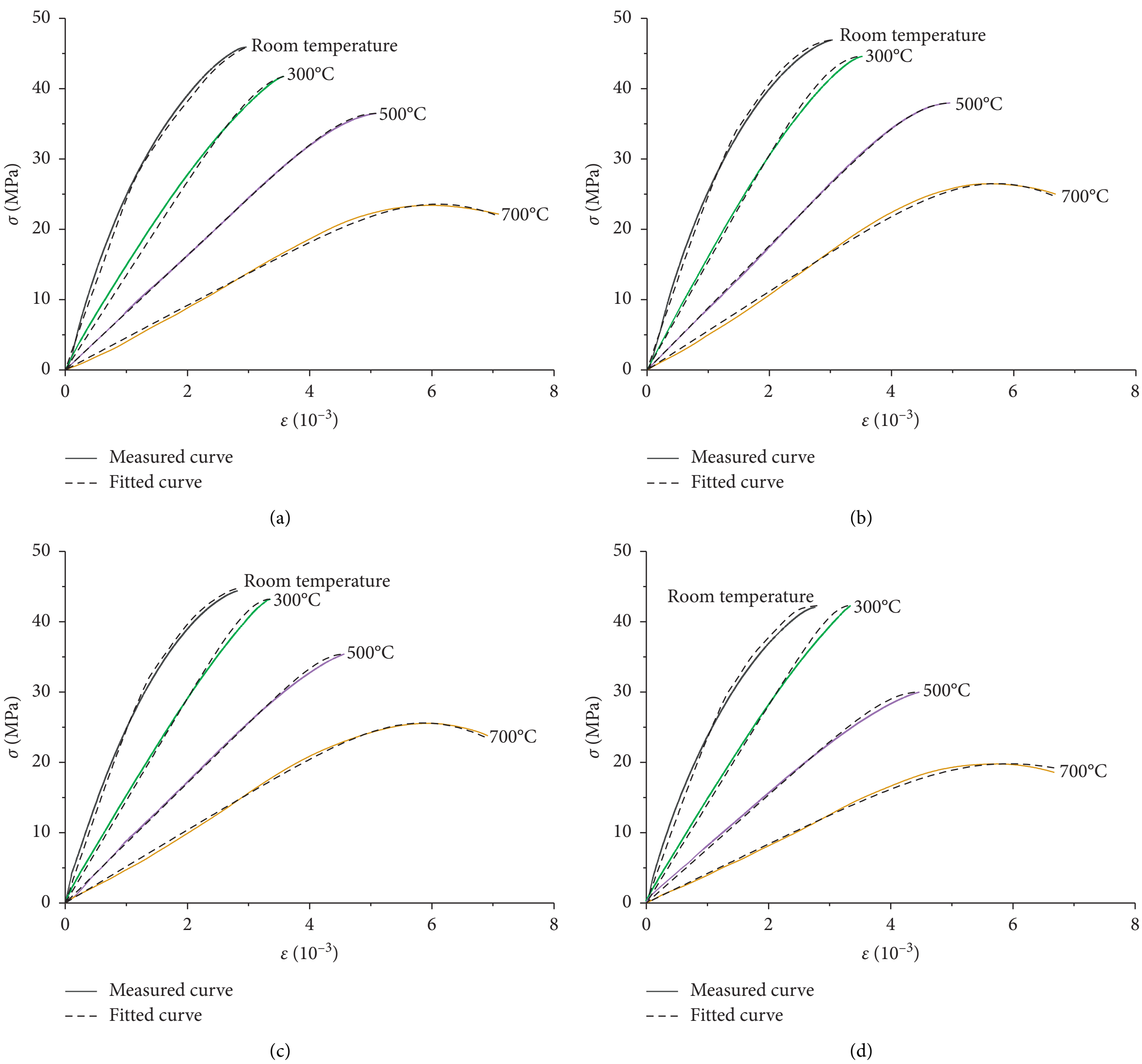

Figure 7: Stress-strain fitting curves of DSM with different DSR after elevated temperature. (a) DSR-20%; (b) DSR-40%; (c) DSR-60%; (d) DSR-80%.

Table 6: Model parameters of coarse aggregate after elevated temperatures [34].

T (°C)	Elastic modulus (GPa)	Peak strain (10^{-3})	Poisson's ratio
20	45	6	0.25
300	50	6	0.25
700	30	6	0.25

a two-dimensional grading curve with equation (8). The number of coarse aggregates can be calculated by equation (9).

$$P(D < D_0) = P_K\left[1.065\left(\frac{D_0}{D_{MAX}}\right)^{0.5} - 0.053\left(\frac{D_0}{D_{MAX}}\right)^{4} - 0.012\left(\frac{D_0}{D_{MAX}}\right)^{6} - 0.0045\left(\frac{D_0}{D_{MAX}}\right)^{8} - 0.0025\left(\frac{D_0}{D_{MAX}}\right)^{10}\right], \quad (8)$$

$$N = \frac{4A}{\pi\overline{D}}, \quad (9)$$

where P_K is percentage of coarse aggregate total volume to the concrete total volume; D_0 is smallest diameter of the coarse aggregate; A is area occupied by coarse aggregate; $\overline{D}$ is average diameter of coarse aggregate; and N is number of coarse aggregates.

3.2.2. A Finite-Element Model of DSC. To produce an acceptable result, at least three test blocks need to be prepared for each case in experiment. In this study, the two-dimensional random aggregate program was written and used. Taking the particle size group with a volume content of 55% and a gradation of 5–10–20 mm as an example, the area occupied by coarse aggregates of 5–10 mm and 10–20 mm can be calculated, respectively. Then, the number of aggregates can be obtained. Therefore, the volume content was ultimately expressed by the number of large and small aggregates. According to Figures 8(a)–8(c), the distribution of large aggregates on the plane was conducted randomly. Figure 8(d) shows the model details. Both cement mortar and coarse aggregate material unit could adopt a quadrilateral four-node plane82 unit, which was divided by a mapped grid.

3.2.3. Comparative Analysis between Experiment and Numerical Simulation. For simulation, the specimen size was $100 \times 100 \times 100$ (mm^3). The coarse aggregate volume content, coarse aggregate particle size, and interface thickness were 55%, 5–10–20 (mm), and 0.6 mm, respectively. Table 7 shows the errors between experimental and simulated results. The errors were tiny and were within ±5%.

Ghannam et al. [40] and Prabhu et al. [41] replaced fine sand with blended granite, iron powder, and foundry sand and found that the optimal replacement rate was 10% and 20%, respectively. In comparison, Al-Jabri et al. [42] suggested that the optimal replacement was 40–50%, when the sand was replaced by copper slag. Therefore, the optimum of fine aggregate was highly dependent on the material type, which was used as a replacement. In Figure 9, the optimal DSR is 40%; it is also shown that the simulated values agree well with the experimental values. Thus, this model was suitable to simulate the uniaxial compression performance of DSC with interface phase after elevated temperature.

In DSC compression process, the initial position of failure was located at the interface inside DSC. With the growth of compressive stress, the DSC specimen was broken in diagonal direction. For failure angle measurement, the lowest failure angle as shown in Figure 10(a) was regarded as failure surface. As shown in Figure 10, after 300°C, the failure modes of DSC in experiments and simulations were compared. The result shows little difference of failure angle between DSC experiment (46.7–49.3°) and simulation (46.6–48.8°), respectively. In three-dimensional view, the failure form of DSC obtained from experiment and simulation was similar to an inverted triangular pyramid.

4. Simulation of Compressive Strength

4.1. Effect of Thickness of Interface Phase on Compressive Strength. Due to computational efficiency problem, it was difficult to adopt micrometers unit scale as the scale of concrete finite element mesoscopic calculation analysis. The thickness of interface phase was 0.2–0.8 mm [25, 43, 44]. Quite a few researchers [27, 45] even assumed that the interface phase thickness was 1 mm or 2 mm in the process of numerical simulation and believed that if the parameters were reasonable enough, it was feasible to expand the thickness of interfacial phase. Zhou and Hao [25] found that the concrete tensile strength declined with increasing interface phase thickness. However, very few studies have been reported on the influence of interface phase thickness on concrete compressive strength. 2D random aggregate distribution program was written and run in ANSYS, which can

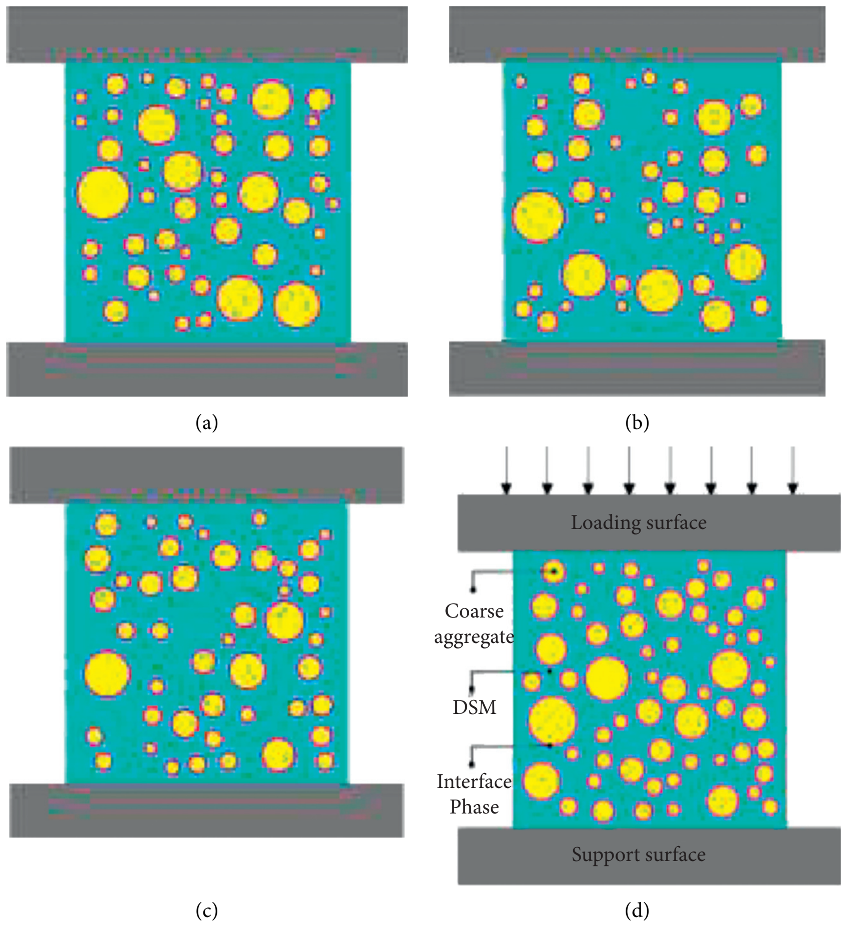

FIGURE 8: Finite element models of DSC. (a) Random distribution—I. (b) Random distribution—II. (c) Random distribution—III. (d) Model details.

TABLE 7: Error between experimental and simulated value (test dates from [39]).

T (°C)	DSR (100% (test-simulation)/test)					
	0%	20%	40%	60%	80%	100%
Room temperature	0.31	0.16	0.00	0.62	0.70	0.07
300	−0.29	1.50	−1.15	0.76	0.94	2.26
500	1.89	0.04	−0.20	3.02	0.43	3.60
700	4.05	3.44	−1.59	0.70	1.49	2.37

simulate the uniaxial compressive failure process of DSC with different interface phase thicknesses. The influence of interface phase thickness on the DSC compressive strength is illustrated in Figure 11. The DSC compressive strength was decreased when interface phase thickness increased.

Through the fitting analysis of three-dimensional surface in Figure 12, for DSC after elevated temperature, the empirical formula between interface phase thickness, temperature, and compressive strength is obtained. As shown in equation (10), the coefficient of determination (R^2) is 0.998, which shows a high degree of fit.

$$\frac{f(T,t)}{f_c} = 1.018 + 0.53\left(\frac{T-20}{700}\right) - 0.026\left(\frac{t}{t_c}\right) - 0.888\left(\frac{T-20}{700}\right)^2, \tag{10}$$

where $f(T,t)$ is DSC compressive strength with different interface phase thickness after elevated temperature; f_c is DSC compressive strength at room temperature; t is interface phase thickness; t_c is maximum value of interface phase thickness.

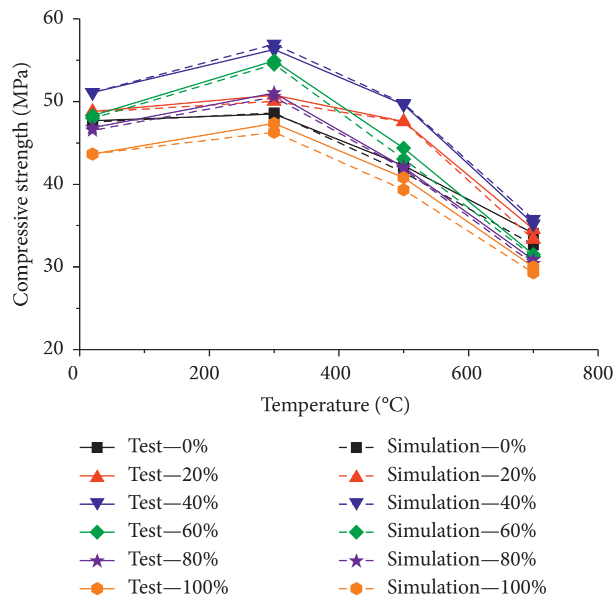

Figure 9: Compressive strength of DSC after elevated temperature.

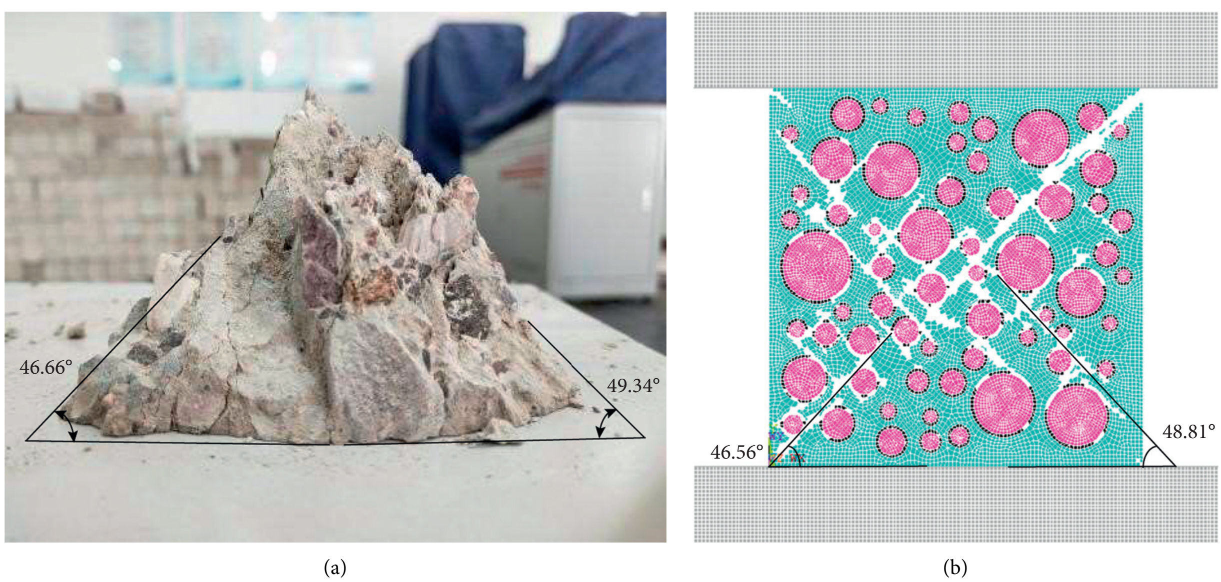

Figure 10: Failure form of DSC. (a) Test; (b) simulation.

4.2. Effect of Compressive Strength of Interface Phase on Compressive Strength of DSC. The mortar compressive strength was obtained from test determining the interface phase compressive strength. It was considered that the strains of mortar and interface phase remained the same, and the interface phase strength was changed by changing the interface phase's elastic modulus. In this study, the interface phase's elastic modulus was assumed to be in the range of 60–90% of the mortar elastic modulus. Table 8 shows the specific values of elastic modulus of interface phase.

The interface phase's thickness was 0.6 mm, particle size group was 5–10–20(mm), DSR was 40%, and coarse aggregate volume content was 45%. According to Figure 13, after elevated temperature, the DSC compressive strength increased with the increase of interface phase's compressive strength. The coefficients of determination (R^2) were larger than 0.99 at different temperatures, which concluded that the interface phase's compressive strength affected the DSC strength significantly.

4.3. Effect of Specimen Size on Compressive Strength. Jin [46] studied the concrete size effect subjected to different strain rates. In the finite element model, volume content of coarse aggregate and particle size were 45% and 5–10–20 mm, respectively. Different sizes of cubes, namely, 100 mm, 150 mm, and 200 mm, were chosen. The uniaxial compression failure processes of DSC after elevated

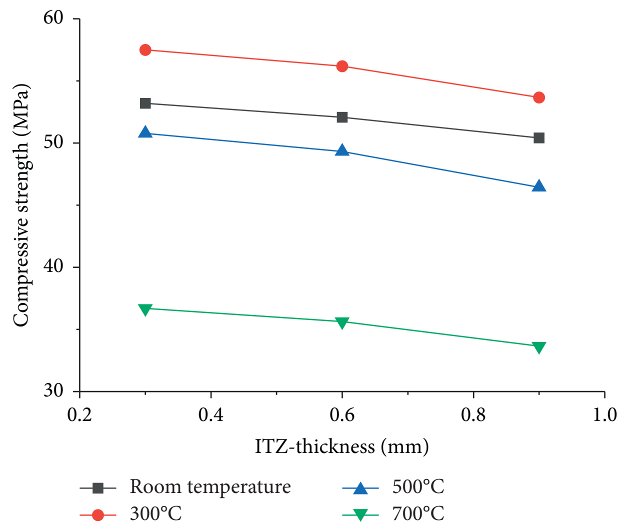

Figure 11: Effect of thickness of interface phase on compressive strength of DSC.

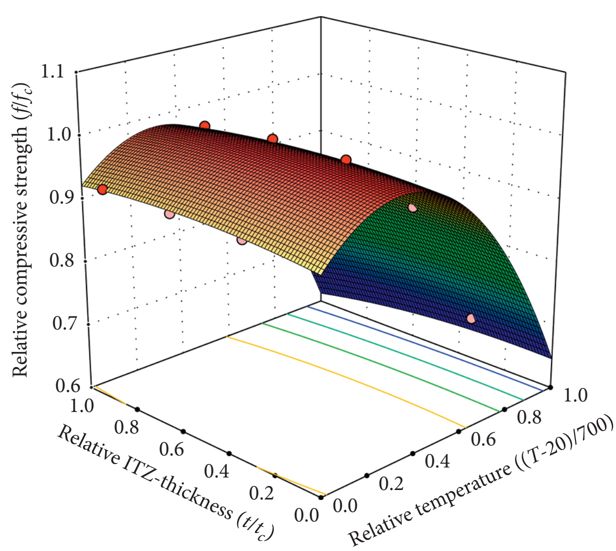

Figure 12: Three-dimensional diagram of interface phase thickness, temperature, and compressive strength of DSC.

Table 8: Compressive strength of interface phase (I-from test; II-for simulation).

T (°C)	Mortar (I)	Interface phase (II)			
		0.6	0.7	0.8	0.9
Room temperature	46.91	28.15	32.84	37.53	42.22
300	44.6	26.76	31.22	35.68	40.14
500	37.91	22.78	26.58	30.38	34.17
700	26.49	15.89	18.54	21.19	23.84

temperatures with varying sizes of specimen were simulated and analysed. In Figure 14, the compressive strength of DSC specimens at different exposure temperatures reduced with the increase of specimen size.

4.4. Effect of Coarse Aggregate Volume Content on Compressive Strength. Meddah et al. [36] found that the coarse aggregate optimal volume content was 45-46%. In Figure 15, the compressive strength of test specimen increased initially

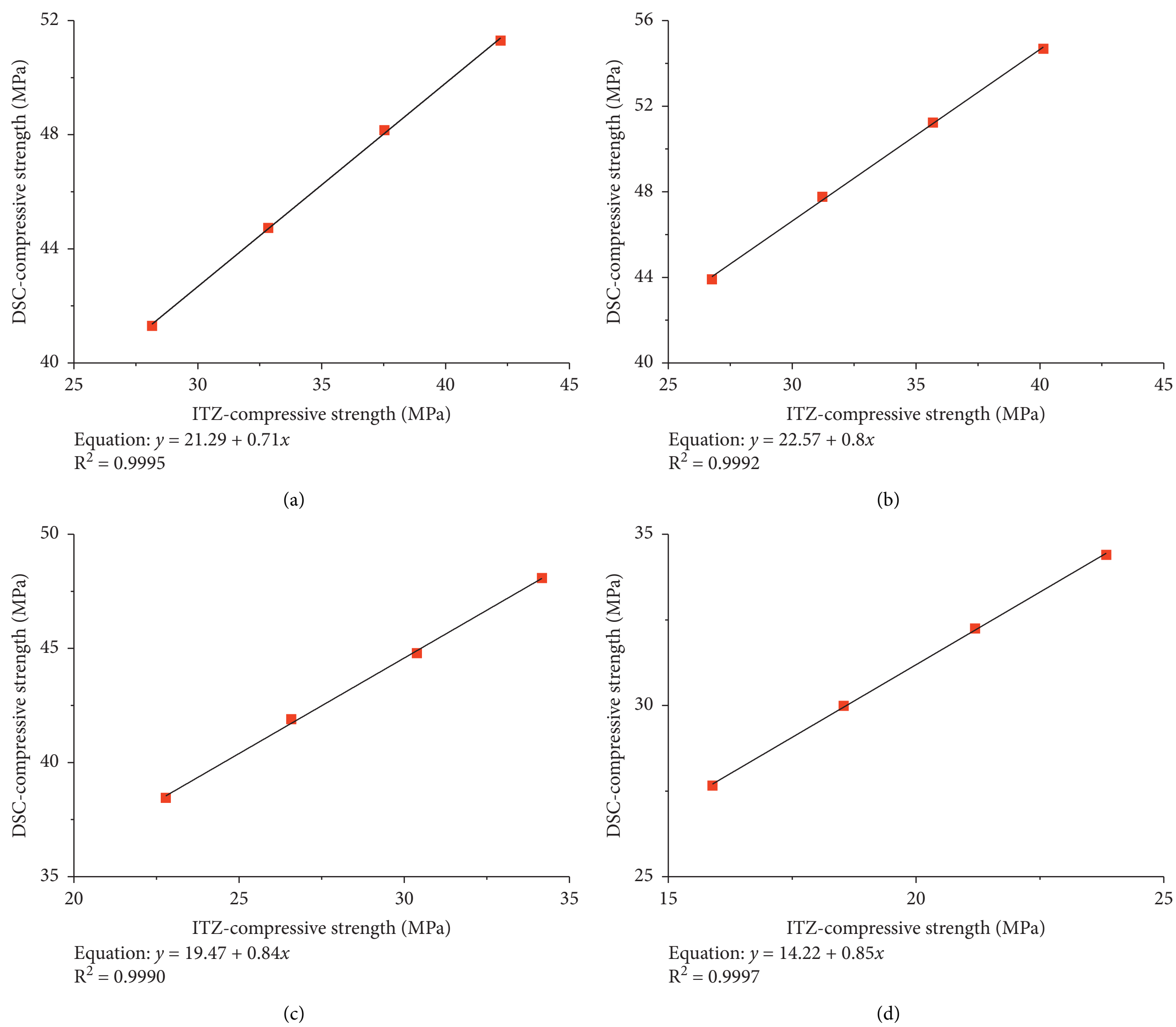

Figure 13: Effect of compressive strength of interface phase on compressive strength of DSC. (a) Room temperature; (b) 300°C; (c) 500°C; (d) 700°C.

and then decreased with the increase of volume content. When the coarse aggregate content was 45%, the DSC compressive strength reached the maximum value.

4.5. Effect of Particle Size of Coarse Aggregate on Compressive Strength. When the aggregate size was selected reasonably, the concrete can obtain good mixing performance, physical properties, and durability [47, 48]. Coarse aggregate particle size had a greater impact on the concrete compressive strength. Ogundipe et al. [49] used single-size aggregates to produce concrete cubes with sizes of 6 mm, 10 mm, 12.5 mm, 20 mm, and 25 mm. The results revealed that the compressive strength began to increase until the aggregate size reached 12.5 mm, and the concrete produced with aggregate size of 20 mm had higher compressive strength than 25 mm. Therefore, the rationality of the choice of aggregate particle size has an important influence on concrete application. The two-graded DSC was prepared, and the effect of minimum, intermediate, and maximum particle sizes on compressive strength of DSC was investigated.

4.5.1. Effect of Minimum Particle Size of Coarse Aggregate on Compressive Strength. The influence of coarse aggregate minimum particle size on the DSC compressive strength was analysed. The particle size was 5–20–25 mm, 10–20–25 mm, and 15–20–25 mm. Therefore, the minimum particle size was 5 mm, 10 mm, and 15 mm, respectively. Figure 16 shows that the DSC compressive strength has the same trend with the rise of minimum size after exposure to different temperatures. The DSC compressive strength declined with increasing the minimum coarse aggregate size.

By fitting the cubic diagram in Figure 17, for DSC after elevated temperature, the empirical formula between minimum particle size, temperature, volume content, and compressive strength is obtained, as shown in equation (11).

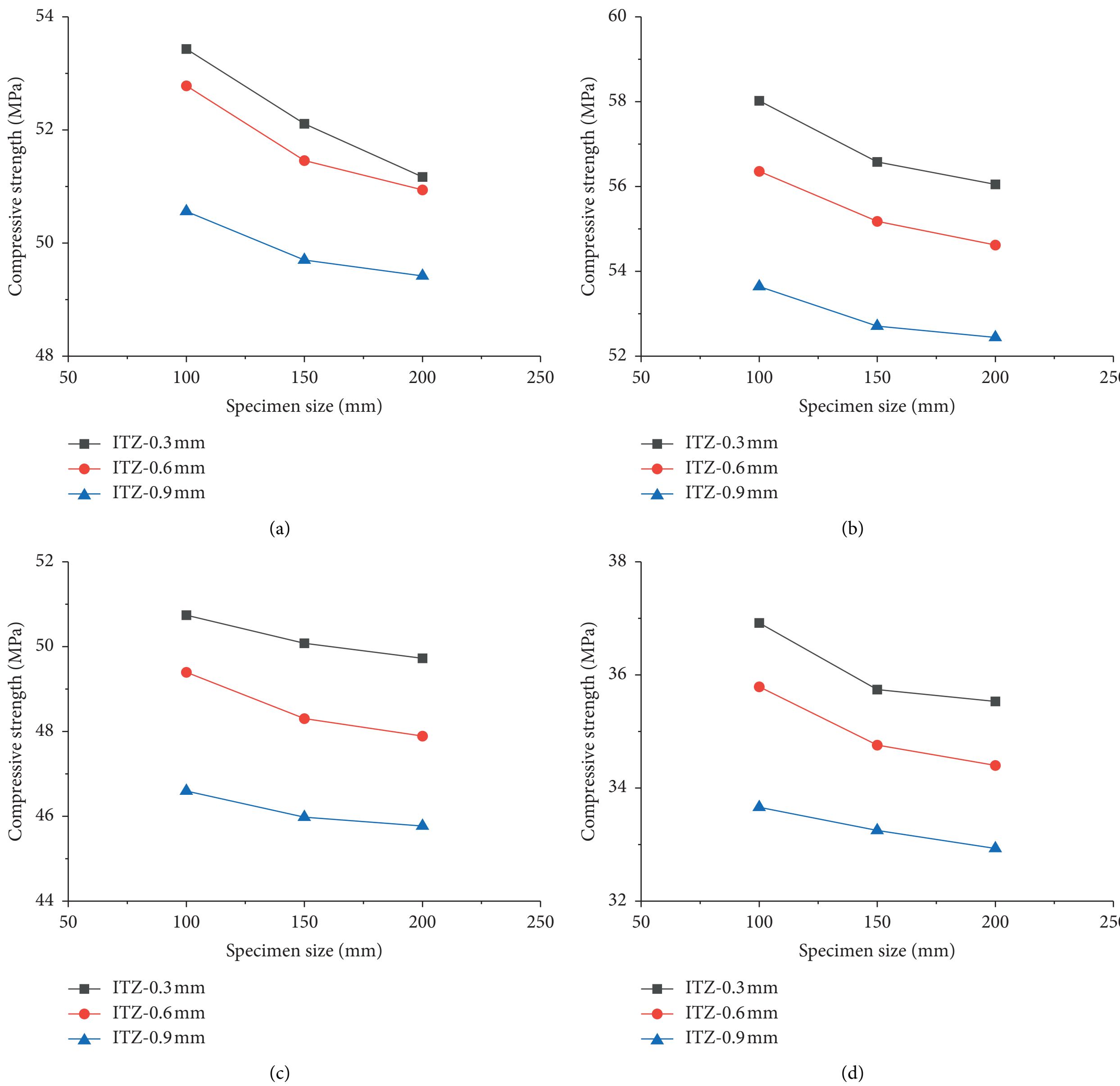

FIGURE 14: Effect of specimen size on compressive strength of DSC. (a) Room temperature; (b) 300°C; (c) 500°C; (d) 700°C.

The determination coefficient (R^2) is 0.999, which has a high degree of fit.

$$\frac{f(T, D_{\min}, V)}{f_c} = 0.99 + 0.59\left(\frac{T-20}{700}\right) - 0.01\left(\frac{D}{D_c}\right) - 0.0003V - 0.02\left(\frac{T-20}{700}\right)\left(\frac{D}{D_c}\right) - 0.94\left(\frac{T-20}{700}\right)^2 + 0.01\left(\frac{D}{D_c}\right)^2, \quad (11)$$

where $f(T, D_{\min}, V)$ is compressive strength considering the influence of temperature, minimum particle size, and volume content; $D_{\min}$ is minimum particle size of two-stage coarse aggregate; V is coarse aggregate volume content; D is particle size of coarse aggregate; D_c is maximum particle size of coarse aggregate in the control group.

4.5.2. Effect of Intermediate Particle Size of Coarse Aggregate on Compressive Strength. The particle size was 5–10–25 mm, 5–15–25 mm, and 5–20–25 mm. Therefore, the intermediate particle size was 10 mm, 15 mm, and 20 mm, respectively. Figure 18 shows the influence of intermediate particle size on the compressive strength of DSC after exposure to elevated

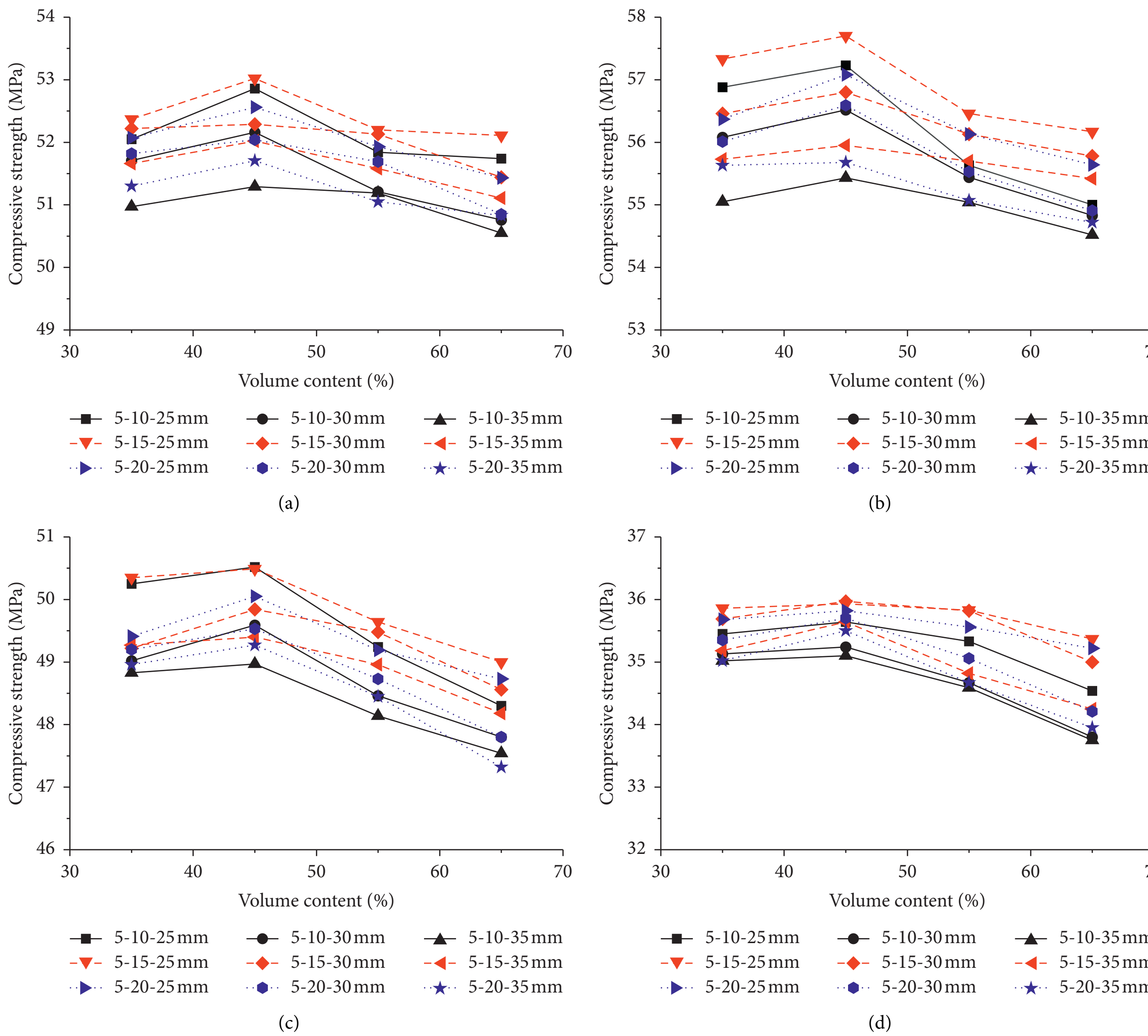

Figure 15: Effect of volume content on compressive strength of DSC. (a) Room temperature; (b)300°C; (c)500°C; (d) 700°C.

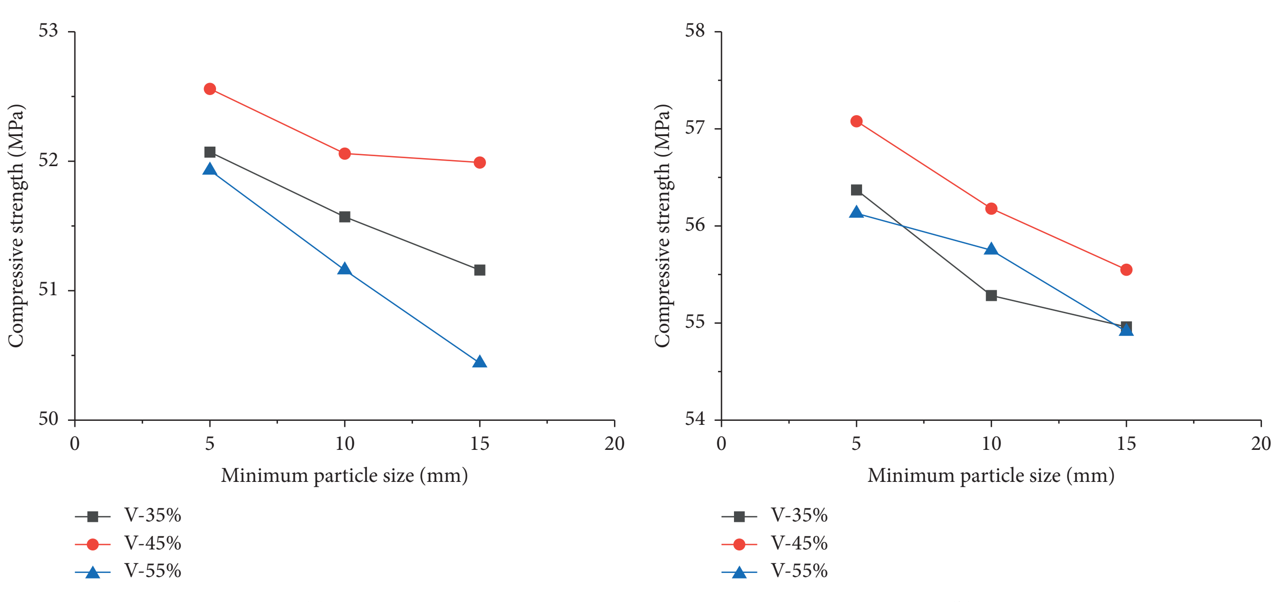

Figure 16: Continued.

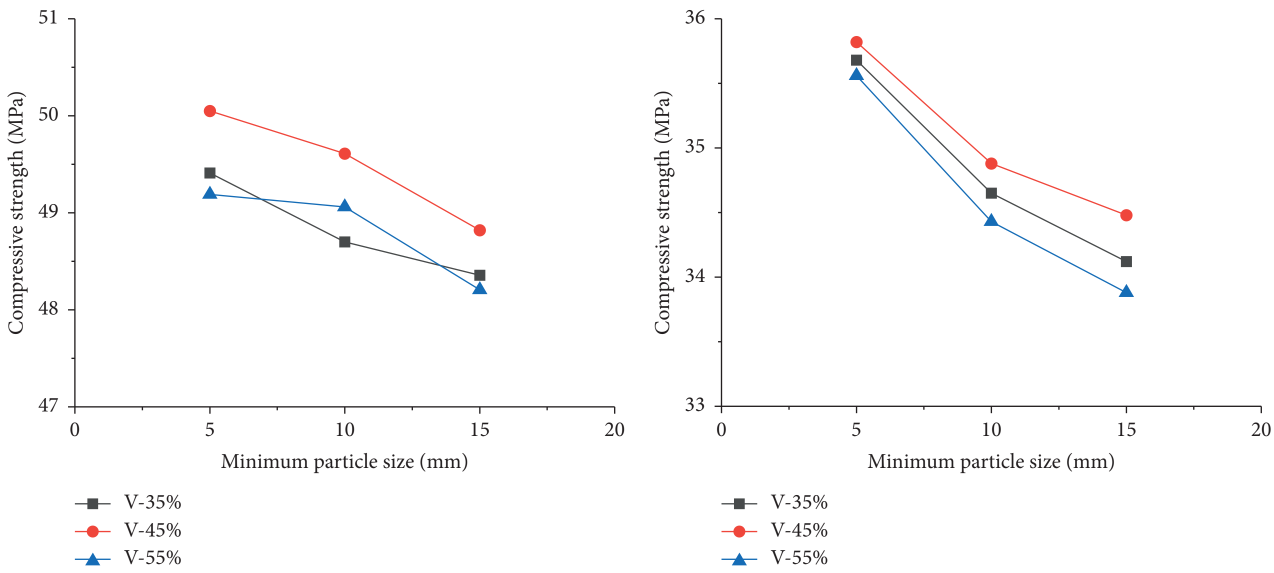

(c)

(d)

Figure 16: Effect of minimum particle size on compressive strength of DSC. (a) Room temperature; (b)300°C; (c)500°C; (d) 700°C.

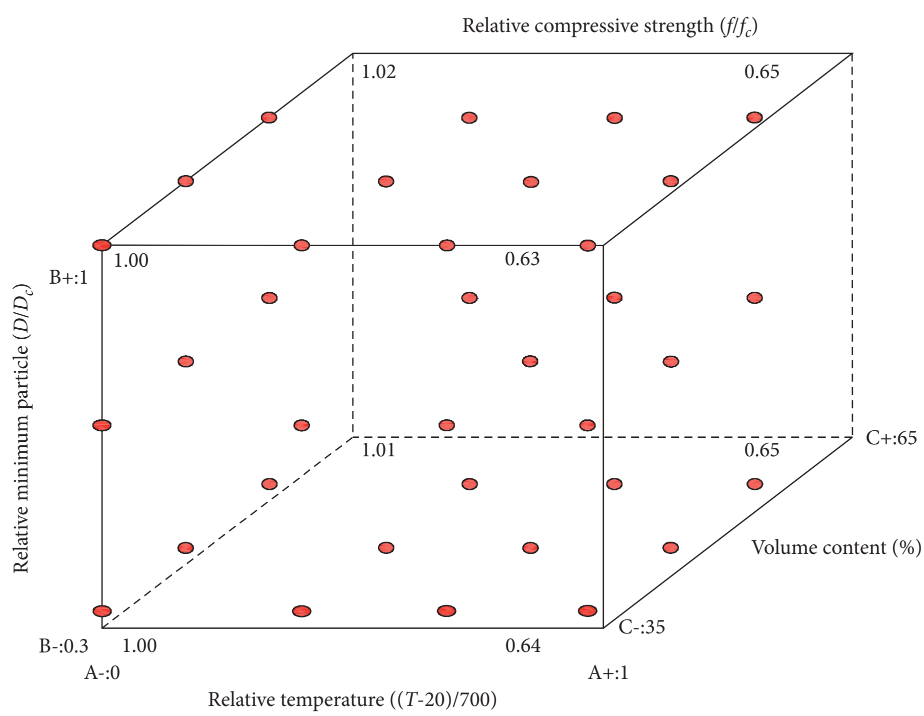

Figure 17: Cube diagram of temperature, volume content, minimum particle size, and compressive strength.

temperatures. As the intermediate particle size gets larger, the compressive strength of DSC increases firstly and then decreases.

By fitting the cubic diagram in Figure 19, the empirical formula between intermediate particle size, temperature, volume content, and compressive strength is obtained, as shown in equation (12). The determination coefficient (R^2) is 0.999, which has a high degree of fit.

$$\frac{f(T, D_{\mathrm{mid}}, V)}{f_c} = 1 + 0.56\left(\frac{T-20}{700}\right) + 0.04\left(\frac{D}{D_c}\right) - 0.0003V + 0.01\left(\frac{T-20}{700}\right)\left(\frac{D}{D_c}\right) - 0.93\left(\frac{T-20}{700}\right)^2 - 0.03\left(\frac{D}{D_c}\right)^2, \quad (12)$$

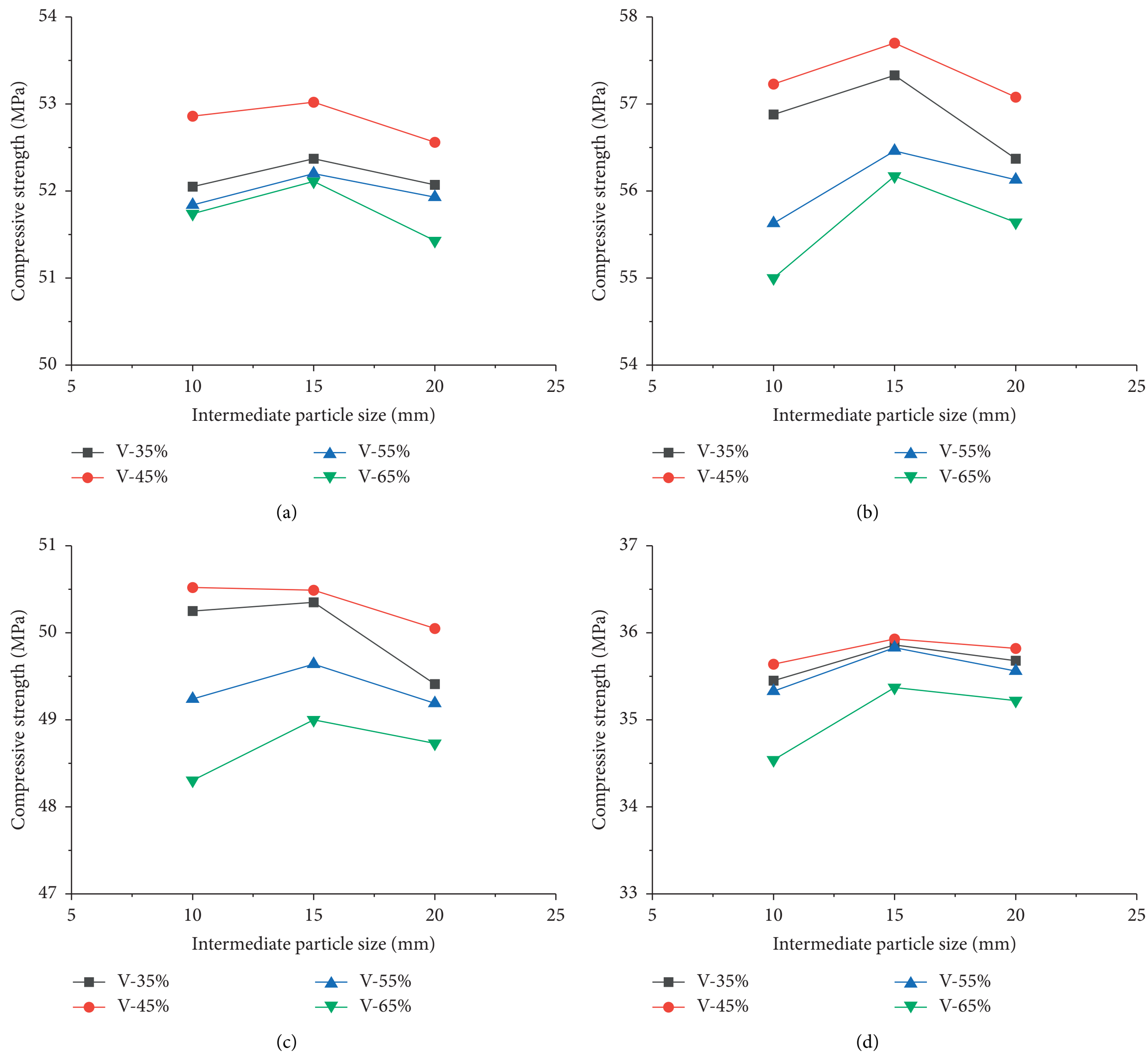

Figure 18: Effect of intermediate particle size on compressive strength of DSC. (a) Room temperature; (b) 300°C; (c) 500°C; (d) 700°C.

where $f(T, D_{\mathrm{mid}}, V)$ is compressive strength considering the influence of temperature, intermediate particle size, and volume content. D_{mid} is intermediate particle size of two-stage coarse aggregate.

4.5.3. Effect of Maximum Particle Size of Coarse Aggregate on Compressive Strength. The particle size was 5–10–15 mm, 5–10–20 mm, 5–10–25 mm, 5–10–30 mm, and 5–10–35 mm. Therefore, the maximum particle size was 15 mm, 20 mm, 25 mm, 30 mm, and 35 mm, respectively. Figure 20 illustrates the influence of the maximum particle size of coarse aggregate on the DSC compressive strength. In Figure 20, as the maximum particle size gets bigger, the compressive strength increases initially and then decreases. When the particle size is 20 mm, the compressive strength reaches the optimal value.

By fitting the cubic diagram in Figure 21, the empirical formula between minimum particle size and temperature, volume content, and compressive strength is obtained, as shown in equation (13). The determination coefficient (R^2) is 0.998, which has a high degree of fit.

$$\frac{f(T, D_{\max}, V)}{f_c} = 1 + 0.59\left(\frac{T-20}{700}\right) - 0.04\left(\frac{D}{D_c}\right) - 0.0002V - 0.02\left(\frac{T-20}{700}\right)\left(\frac{D}{D_c}\right) - 0.93\left(\frac{T-20}{700}\right)^2 + 0.03\left(\frac{D}{D_c}\right)^2, \tag{13}$$

where $f(T, D_{\max}, V)$ is compressive strength considering the influence of temperature, maximum particle size, and volume content. $D_{\max}$ is maximum particle size of a two-stage coarse aggregate.

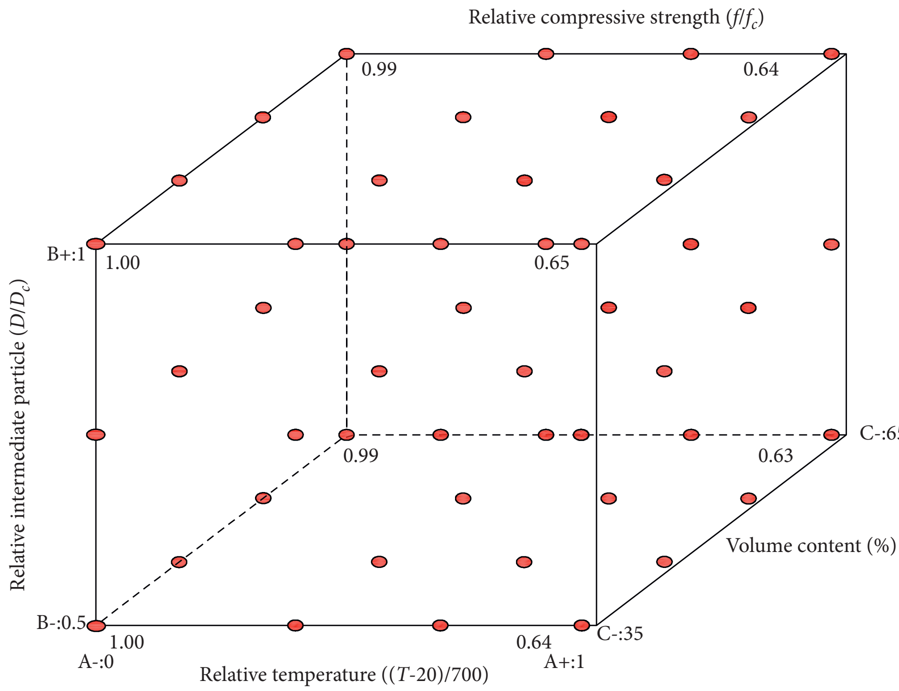

FIGURE 19: Cube diagram of temperature, volume content, intermediate particle size, and compressive strength.

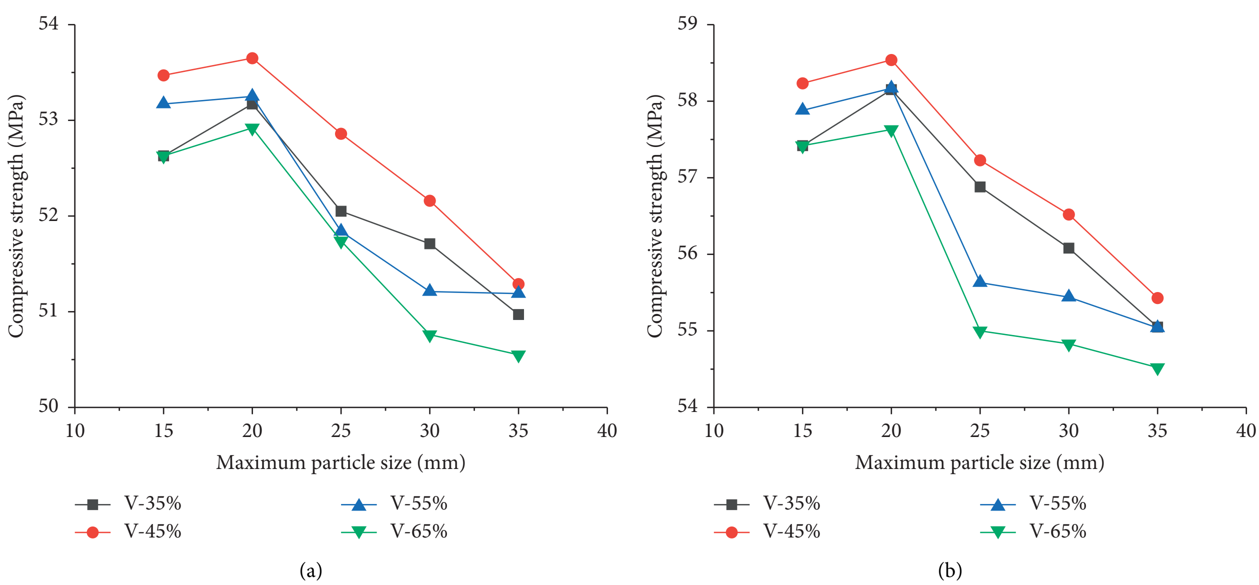

FIGURE 20: Continued.

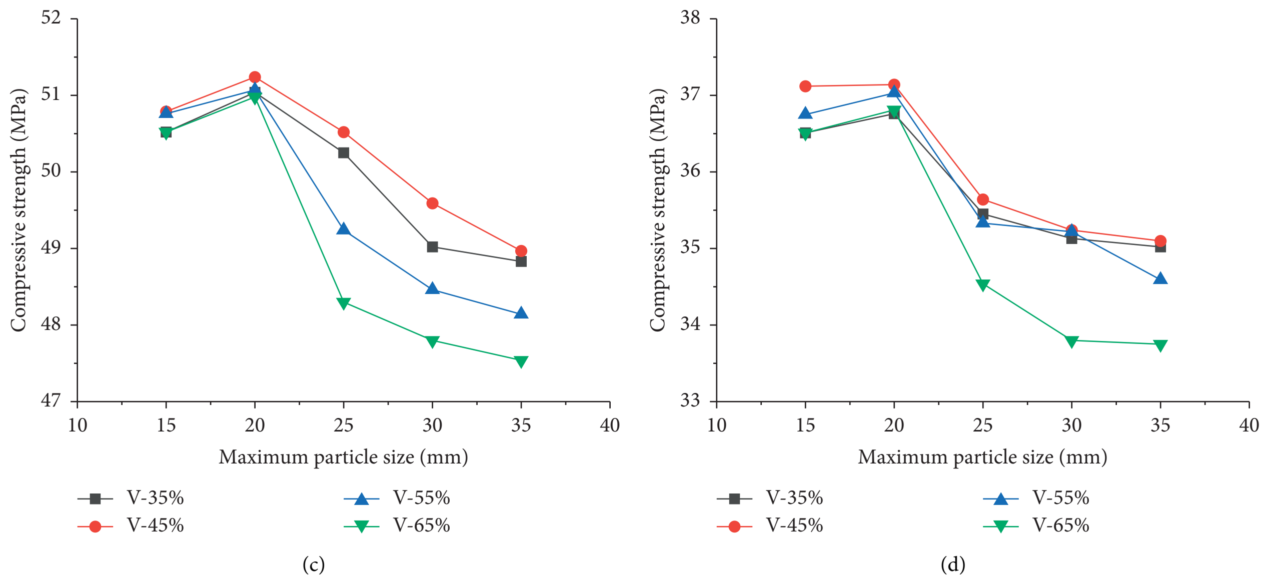

Figure 20: Effect of maximum particle size on compressive strength of DSC. (a) Room temperature; (b) 300°C; (c) 500°C; (d) 700°C.

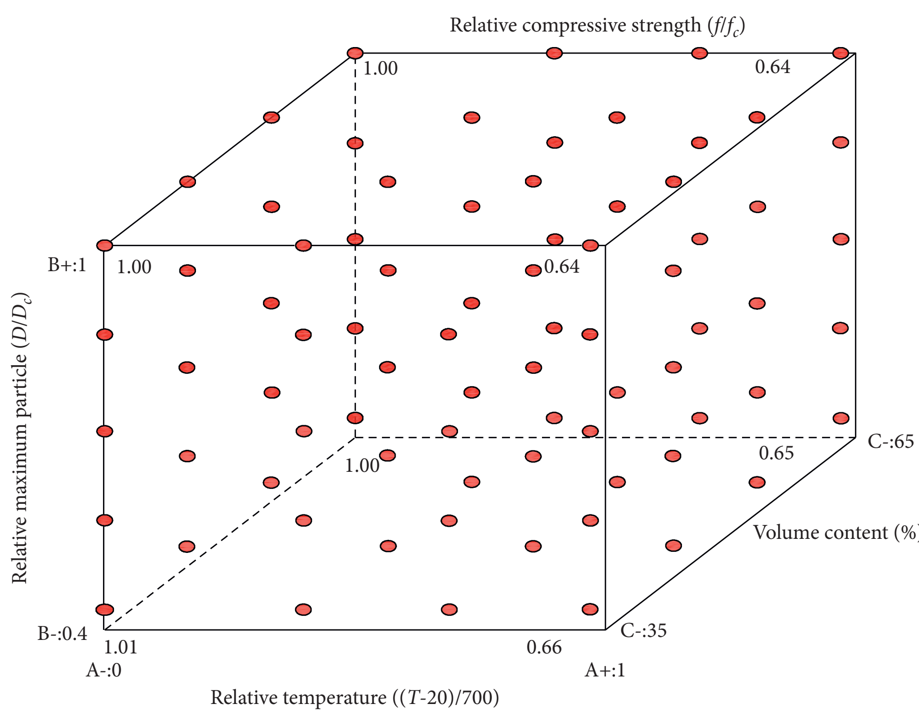

Figure 21: Cube diagram of temperature, volume content, maximum particle size, and compressive strength.

5. Conclusions

The mechanical properties and model of DSM after elevated temperature were obtained through experiments, which provided material parameters for subsequent simulation, and ANSYS software was used to research compression failure process of DSC with interface phase. The effects of interface phase thickness, interface phase compressive strength, test specimen size, volume content, and particle size on the DSC compressive strength after elevated temperature were analysed. The conclusions were as follows:

(1) The DSC compressive strength decreased when the thickness of interface phase changed from 0.3 mm to 0.9 mm. After elevated temperature, the DSC compressive strength had a linearly increasing relationship with the interface phase's compressive

strength. The DSC compressive strength decreased with the increase of specimen size.

(2) The compressive strength of specimen at different temperatures increased firstly and then decreased with increasing coarse aggregate volume. The compressive strength reached the peak value when the volume content was 45%. When the temperature reached 700°C, the effect of volume content of coarse aggregate on compressive strength of DSC was significantly weakened.

(3) The DSC compressive strength reduced with increasing minimum particle size. With the growth of coarse aggregate intermediate and maximum particle size, the compressive strength increased firstly and then decreased. For maximum particle size, when the particle size was 20 mm, the compressive strength reached the optimal value. Compared to the intermediate particle size, the minimum and maximum particle sizes had more significant impacts on the DSC compressive strength.

Based on this study, the constitutive model of DSM and numerical simulation results can provide the support for the fire resistance of DSC.

Data Availability

The data and materials used in the study are included in the article.

Conflicts of Interest

The authors declare that they have no conflicts of interest.

Acknowledgments

The work described in this paper was fully supported by the Science Foundation of Ningxia (2020AAC03044 and 2020AAC03041), the National Natural Science Foundation of China (nos. 11162015 and 51408328), the Scientific and Technological Research Project of Institutions of Higher Learning in Ningxia (NGY2020104), and First Class Discipline Construction in Ningxia Colleges and Universities (discipline of water conservancy engineering) (NXYLXK 2021A03).

References

[1] Chinese Yearbook, *China Fire Services 2013*, China Personnel Press, Beijing, China, 2013.

[2] Chinese Yearbook, *China Fire Services 2014*, Yunnan People's Publishing House, Yunnan, China, 2014.

[3] Chinese Yearbook, *China Fire Services 2015*, Yunnan People's Publishing House, Yunnan, China, 2016.

[4] W. Jung, M. Kwon, and B. Ju, "Evaluation of compressive strength of concrete members laterally confined by various FRP composites and exposed to high temperatures," *KSCE Journal of Civil Engineering*, vol. 20, no. 6, pp. 2410–2419, 2016.

[5] H. M. Mahmod, A. A. F. N. Aznieta, and S. J. Gatea, "Evaluation of rubberized fibre mortar exposed to elevated temperature using destructive and non-destructive testing," *KSCE Journal of Civil Engineering*, vol. 21, no. 4, pp. 1347–1358, 2017.

[6] P. Pliya, D. Cree, H. Hajiloo, A.-L. Beaucour, M. F. Green, and A. Noumowé, "High-strength concrete containing recycled coarse aggregate subjected to elevated temperatures," *Fire Technology*, vol. 55, no. 5, pp. 1477–1494, 2019.

[7] P. Qiu, "Experimental research on fracture behavior of concrete after high temperature," *Frattura Ed Integrità Strutturale*, vol. 13, no. 50, pp. 300–309, 2019.

[8] Y. Esen and A. Kurt, "Effect of high temperature in concrete for different mineral additives and rates," *KSCE Journal of Civil Engineering*, vol. 22, no. 4, pp. 1288–1294, 2018.

[9] J. Dragas, I. Ignjatovic, N. Tosic, and S. Marinkovic, "Mechanical and time-dependent properties of high-volume fly ash concrete for structural use," *Magazine of Concrete Research*, vol. 68, no. 12, pp. 632–645, 2016.

[10] N. Biglarijoo, M. Nili, S. M. Hosseinian, M. Razmara, S. Ahmadi, and P. Razmara, "Modelling and optimisation of concrete containing recycled concrete aggregate and waste glass," *Magazine of Concrete Research*, vol. 69, no. 6, pp. 306–316, 2017.

[11] M. Zhang, H. Liu, S. Sun, X. Chen, and S. I. Doh, "Dynamic mechanical behaviors of desert sand concrete (DSC) after different temperatures," *Applied Sciences*, vol. 9, no. 19, p. 4151, 2019.

[12] H. F. Liu, J. R. Ma, Y. Y. Wang, and J. G. Ning, "Influence of desert sand on the mechanical properties of concrete subjected to impact loading," *Acta Mechanica Solida Sinica*, vol. 30, no. 6, pp. 583–595, 2017.

[13] J. Che, D. Wang, H. Liu, and Y. Zhang, "Mechanical properties of desert sand-based fiber reinforced concrete (DSFRC)," *Applied Sciences*, vol. 9, no. 9, p. 1857, 2019.

[14] G. X. Zhang and J. S. Yang, "Research on engineering characteristics of Tenggeli desert sand," *Highway*, vol. s1, pp. 131–134, 2003.

[15] N. Wang and B. Li, "Cooperating ratio design and research of Sahara desert sand high-strength concrete," *Concrete*, vol. 39, pp. 139–146, 2014.

[16] China Industrial Construction Press, *Design Specification for Mix Ratio of Ordinary Concrete (JGJ55-2011)*, China Industrial Construction Press, Beijing, China, 2011.

[17] W. Yan, G. Wu, and Z. Dong, "Optimization of the mix proportion for desert sand concrete based on a statistical model," *Construction and Building Materials*, vol. 226, pp. 469–482, 2019.

[18] X. Yu, L. Chen, Q. Fang, Z. Ruan, J. Hong, and H. Xiang, "A concrete constitutive model considering coupled effects of high temperature and high strain rate," *International Journal of Impact Engineering*, vol. 101, pp. 66–77, 2017.

[19] L. Marsavina, K. Audenaert, G. De Schutter, N. Faur, and D. Marsavina, "Experimental and numerical determination of the chloride penetration in cracked concrete," *Construction and Building Materials*, vol. 23, no. 1, pp. 264–274, 2009.

[20] S. Albrifkani and Y. C. Wang, "Explicit modelling of large deflection behaviour of restrained reinforced concrete beams in fire," *Engineering Structures*, vol. 121, pp. 97–119, 2016.

[21] G. Morales-Alonso, V. Rey-de-Pedraza, F. Cendón, and D. A. Cendon, "Numerical simulation of fracture of concrete at different loading rates by using the cohesive crack model," *Theoretical and Applied Fracture Mechanics*, vol. 96, pp. 308–325, 2018.

[22] H. F. Liu and P. Wu, “Dynamic characteristics of concrete with different interfacial phase thickness,” *Chinese Journal of High Pressure Physics*, vol. 31, no. 3, pp. 249–260, 2017.

[23] S. Zhang, C. Zhang, L. Liao, and C. Wang, “Numerical study of the effect of ITZ on the failure behaviour of concrete by using particle element modelling,” *Construction and Building Materials*, vol. 170, pp. 776–789, 2018.

[24] C. Zhang, X. Yang, and H. Gao, “Effect of randomness of interfacial properties on fracture behavior of concrete under uniaxial tension,” *Acta Mechanica Solida Sinica*, vol. 31, no. 2, pp. 174–186, 2018.

[25] X. Q. Zhou and H. Hao, “Modelling of compressive behaviour of concrete-like materials at high strain rate,” *International Journal of Solids and Structures*, vol. 45, no. 17, pp. 4648–4661, 2008.

[26] K. L. Scrivener, A. K. Crumbie, and P. Laugesen, “The interfacial transition zone (ITZ) between cement paste and aggregate in concrete,” *Interface Science*, vol. 12, no. 4, pp. 411–421, 2004.

[27] L. Jin, C. Xu, Y. Han, and X. Du, “Effect of end friction on the dynamic compressive mechanical behavior of concrete under medium and low strain rates,” *Shock and Vibration*, vol. 2016, pp. 1–20, 2016.

[28] W. Xu, Z. Han, L. Tao, Q. Ding, and H. Ma, “Random non-convex particle model for the fraction of interfacial transition zones (ITZs) in fully-graded concrete,” *Powder Technology*, vol. 323, pp. 301–309, 2018.

[29] Shanxi Provincial Academy of Building Sciences, *Standard for Test Methods of Basic Performance of Building Mortar (JCJ/T70-2009)*, China Industrial Construction Press, Beijing, China, 2009.

[30] S. Sun and H. F. Liu, “Experimental study on splitting tensile strength of desert sand concrete after high temperature,” *Industrial Construction*, vol. 49, no. 1, pp. 140–169, 2019.

[31] M. Xu, T. Wang, and Z. F. Chen, “Experimental study on the uniaxial compression stress-strain relationship of recycled mortar after high temperature,” *Journal of Building Structures*, vol. 36, no. 2, pp. 151–157, 2015.

[32] H. F. Liu, X. L. Chen, J. L. Che, N. Liu, and M. H. Zhang, “Mechanical performances of concrete produced with desert sand after elevated temperature,” *International Journal of Concrete Structures and Materials*, vol. 14, no. 1, pp. 1–15, 2020.

[33] S. Popovics, “A numerical approach to the complete stress-strain curve of concrete,” *Cement and Concrete Research*, vol. 3, no. 5, pp. 583–599, 1973.

[34] G. Wu, N. G. Teng, and Y. Wang, “Physical and mechanical characteristics of limestone after high temperature,” *Chinese Journal of Geotechnical Engineering*, vol. 33, no. 2, pp. 259–264, 2011.

[35] T. Akcaoglu, M. Tokyay, and T. Celik, “Effect of coarse aggregate size and matrix quality on ITZ and failure behavior of concrete under uniaxial compression,” *Cement & Concrete Composites*, vol. 26, no. 6, pp. 633–638, 2004.

[36] M. S. Meddah, S. Zitouni, and S. Belâabes, “Effect of content and particle size distribution of coarse aggregate on the compressive strength of concrete,” *Construction and Building Materials*, vol. 24, no. 4, pp. 505–512, 2010.

[37] W. B. Fuller and S. E. Thompson, “The laws of proportioning concrete,” *Journal of Transportation Division*, vol. 59, no. 1, pp. 67–143, 1907.

[38] J. C. Walaraven and H. W. Reinhardt, “Theory and experiments on the mechanical behavior of cracks in plain and reinforced concrete subjected to shear loading,” *Heron*, vol. 26, no. 1, pp. 23–33, 1991.

[39] N. Liu, “Study on the mechanical behavior of desert sand concrete after high temperature,” Master’s Thesis, Ningxia University, Yinchuan, China, 2018.

[40] S. Ghannam, H. Najm, and R. Vasconez, “Experimental study of concrete made with granite and iron powders as partial replacement of sand,” *Sustainable Materials and Technologies*, vol. 9, pp. 1–9, 2016.

[41] G. G. Prabhu, J. H. Hyun, and Y. Y. Kim, “Effects of foundry sand as a fine aggregate in concrete production,” *Construction and Building Materials*, vol. 70, pp. 514–521, 2014.

[42] K. S. Al-Jabri, A. H. Al-Saidy, and R. Taha, “Effect of copper slag as a fine aggregate on the properties of cement mortars and concrete,” *Construction and Building Materials*, vol. 25, no. 2, pp. 933–938, 2011.

[43] R. R. Pedersen, A. Simone, and L. J. Sluys, “Mesoscopic modeling and simulation of the dynamic tensile behavior of concrete,” *Cement and Concrete Research*, vol. 50, pp. 74–87, 2013.

[44] Y. Huang, Z. Yang, W. Ren, G. Liu, and C. Zhang, “3D meso-scale fracture modelling and validation of concrete based on in-situ X-ray computed tomography images using damage plasticity model,” *International Journal of Solids and Structures*, vol. 68, pp. 340–352, 2015.

[45] X. Du, L. Jin, and R. Zhang, “Modeling the cracking of cover concrete due to non-uniform corrosion of reinforcement,” *Corrosion Science*, vol. 89, pp. 189–202, 2014.

[46] L. Jin, W. X. Yu, and X. L. Du, “Study on the size effect of concrete dynamic compressive strength based on micro-simulation,” *Engineering Mechanics*, vol. 36, no. 11, pp. 189–202, 2019.

[47] Y.-J. Lee, J.-M. Lee, C.-J. Wang, S.-W. Kim, H.-G. Kim, and K.-H. Kim, “Compressive stress distribution of concrete with EAF oxidising slag aggregates,” *Magazine of Concrete Research*, vol. 70, no. 7, pp. 365–378, 2018.

[48] M. Elices and C. G. Rocco, “Effect of aggregate size on the fracture and mechanical properties of a simple concrete,” *Engineering Fracture Mechanics*, vol. 75, no. 13, pp. 3839–3851, 2008.

[49] O. M. Ogundipe, A. O. Olanike, E. S. Nnochiri, and P. O. Ale, “Development of soil distribution and liquefaction potential maps for downtown area in Yangon, Myanmar,” *Civil Engineering Journal*, vol. 4, no. 4, pp. 836–842, 2018.